



**HAL**  
open science

## Electron paramagnetic resonance of Fe<sup>3+</sup> in gallium borate: Superposition model analysis

Kira Seleznyova, Mark Strugatsky, Sergey Yagupov, Natalia Postivey, Alla Artemenko, Janis Kliava

► **To cite this version:**

Kira Seleznyova, Mark Strugatsky, Sergey Yagupov, Natalia Postivey, Alla Artemenko, et al.. Electron paramagnetic resonance of Fe<sup>3+</sup> in gallium borate: Superposition model analysis. *physica status solidi (b)*, 2014, 251 (7), pp.1393-1400. 10.1002/pssb.201350359 . hal-01064076

**HAL Id: hal-01064076**

**<https://hal.science/hal-01064076>**

Submitted on 26 Feb 2018

**HAL** is a multi-disciplinary open access archive for the deposit and dissemination of scientific research documents, whether they are published or not. The documents may come from teaching and research institutions in France or abroad, or from public or private research centers.

L'archive ouverte pluridisciplinaire **HAL**, est destinée au dépôt et à la diffusion de documents scientifiques de niveau recherche, publiés ou non, émanant des établissements d'enseignement et de recherche français ou étrangers, des laboratoires publics ou privés.



Distributed under a Creative Commons Attribution - NonCommercial 4.0 International License

# Electron paramagnetic resonance of Fe<sup>3+</sup> in gallium borate: Superposition model analysis

Kira Seleznyova<sup>1,2</sup>, Mark Strugatsky<sup>2</sup>, Sergey Yagupov<sup>2</sup>, Natalia Postivey<sup>2</sup>, Alla Artemenko<sup>3</sup>, and Janis Kliava<sup>\*,1</sup>

<sup>1</sup> LOMA, UMR 5798, Université de Bordeaux CNRS, 33405 Talence Cedex, France

<sup>2</sup> Taurida National University, 4 Vernadsky Ave, 95007 Simferopol, Ukraine

<sup>3</sup> ICMCB, UPR CNRS 9048, 33608 Pessac Cedex, France

**Keywords** Fe<sup>3+</sup> electron paramagnetic resonance, gallium borate, spin Hamiltonian, superposition model

---

\* Corresponding author: e mail j.kliava@loma.u bordeaux1.fr, Phone: +33 5 40 00 61 72, Fax: +33 5 40 00 96 70

A series of high quality Fe<sub>x</sub>Ga<sub>1-x</sub>BO<sub>3</sub> single crystals with  $0 \leq x \leq 1$  was prepared and studied by electron magnetic resonance in the temperature range from 4 to 290 K. At low  $x$ , only the electron paramagnetic resonance (EPR) of diluted Fe<sup>3+</sup> ions is present. The EPR spectra for different orientations of the magnetizing field have been computer simulated. With a conventional spin Hamiltonian including the Zeeman and fine structure terms, two different sets of best fit parameters have

been found. This ambiguity has been resolved on the basis of the general spin Hamiltonian with parameters determined from the crystallographic data using the Newman superposition model. A detailed fitting to the experimental EPR spectra assuming statistical distributions of Fe<sup>3+</sup> ligand coordinates has revealed the existence of a certain degree of local disorder in Fe<sub>x</sub>Ga<sub>1-x</sub>BO<sub>3</sub> single crystals.

**1 Introduction** Iron borate FeBO<sub>3</sub> is an extraordinary material – one of the few that combine room temperature magnetic ordering and high transparency up to the near ultraviolet spectral range. The synthesis of FeBO<sub>3</sub> single crystals and the determination of their crystal structure were first reported by Bernal et al. [1]. FeBO<sub>3</sub> has a rhombohedral calcite structure with  $D_{3d}^6$  space group. The structural parameters were later refined by Diehl et al. [2, 3]. From the magnetic point of view, FeBO<sub>3</sub> is a two sublattice easy-plane antiferromagnetic with the Néel temperature  $T_N = 348$  K [4]. Besides, a canting of the sublattice magnetizations produces an in-plane weak ferromagnetism. The crystalline and magnetic structure as well as a strong magnetoelastic coupling in FeBO<sub>3</sub> give rise to a number of interesting characteristics: magnetic [5-9], optical and magneto-optical [10-14], acoustic and acoustooptical [15], magneto-acoustical [16, 17], Mössbauer effect [5, 18], and magnetic resonance [19, 20].

The physical characteristics of the iron borate system can be radically modified through diamagnetic dilution, i.e., isomorphous substitution of a part of iron with different

diamagnetic ions. This is due to difference in dependence on iron concentration of mechanisms behind these characteristics. Besides, diamagnetic dilution is a powerful technique allowing comprehensive studies of transformation from paramagnetic to magnetically ordered state. On the other hand, varying the concentration of diamagnetic ions in the course of crystal synthesis offers the possibility to fine-tune their properties and thus create new materials suitable for various technical applications.

Because of similarity of its ionic radius with that of iron, gallium seems to be the best candidate for achieving the diamagnetic dilution. Recently, some of the present authors have developed a synthesis technique and have prepared Fe<sub>x</sub>Ga<sub>1-x</sub>BO<sub>3</sub> single crystals of high quality in the whole range of  $x$  values,  $0 \leq x \leq 1$  [21] and have analysed them by X-ray fluorescence technique [22], energy-dispersive X-ray spectroscopy, optical absorption, and magnetic circular dichroism [23, 24].

From the viewpoint of magnetic properties, mixed gallium-iron borates represent a model system allowing one to monitor a gradual passage from isolated paramagnetic

ions through magnetic clusters towards an antiferromagnetically coupled lattice. One of the most powerful techniques allowing to study this transformation is without doubt the electron magnetic resonance (EMR). We are using the EMR term as a generic one to refer to any type of magnetic resonance involving the electronic system, i.e., electron paramagnetic resonance (EPR), ferromagnetic resonance, antiferromagnetic resonance (AFMR), etc. In this paper, we mainly focus on the EPR, i.e., the EMR of diluted paramagnetic ions. We present a detailed account of experimental EPR studies of  $\text{Fe}_x\text{Ga}_{1-x}\text{BO}_3$  single crystals with low Fe contents and provide a quantitative description of the EPR spectra through accurate computer simulations.

**2 Experimental details** A series of iron-gallium borate single crystals has been synthesized in  $\text{Ga}_2\text{O}_3$ - $\text{Fe}_2\text{O}_3$ - $\text{B}_2\text{O}_3$ - $\text{PbO}$ - $\text{PbF}_2$  system with  $\text{B}_2\text{O}_3$ ,  $\text{PbO}$ , and  $\text{PbF}_2$  as solvents. Optimal component ratios in the charge and temperature modes were determined by differential thermal analysis [25].

The synthesized  $\text{Fe}_x\text{Ga}_{1-x}\text{BO}_3$  crystals for various  $x$  are shown in Fig. 1. The crystals have the shape of thin hexagonal plates making 0.1–0.3 mm along the trigonal  $C_3$  axis and up to 5 mm in the basal plane perpendicular to the  $C_3$  axis (see Ref. [3] for the axes definition).

The crystals were studied by EMR with an X-band (9.464 GHz) spectrometer (Bruker) in the temperature range from 4 to 290 K and static magnetic fields  $B$  up to 1 T. The EPR spectra were computer simulated using laboratory-developed codes.

**3 Results and discussion** Depending on the iron contents and the temperature, several types of EMR have been observed in  $\text{Fe}_x\text{Ga}_{1-x}\text{BO}_3$  crystals. Figure 2 shows the spectra shapes at different  $x$ -values. At  $x = 0.003$ , curve a, only EPR of diluted  $\text{Fe}^{3+}$  ions is present. For crystals with  $x = 0.04$ , curve b, the EPR lines are broadened due to dipole-dipole interaction. At  $x = 0.2$ , curve c, the EPR of diluted ions disappears and a single broad line of Lorentzian shape occurs, with the effective  $g$ -value about 2.0. This line has

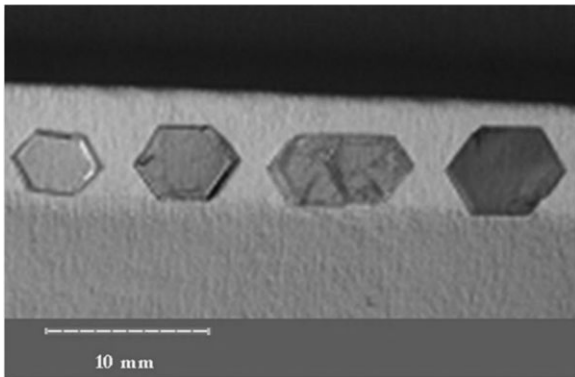


**Figure 1** From left to right:  $\text{Fe}_x\text{Ga}_{1-x}\text{BO}_3$  crystals with  $x = 0, 0.05, 0.20,$  and  $1.0,$  respectively.

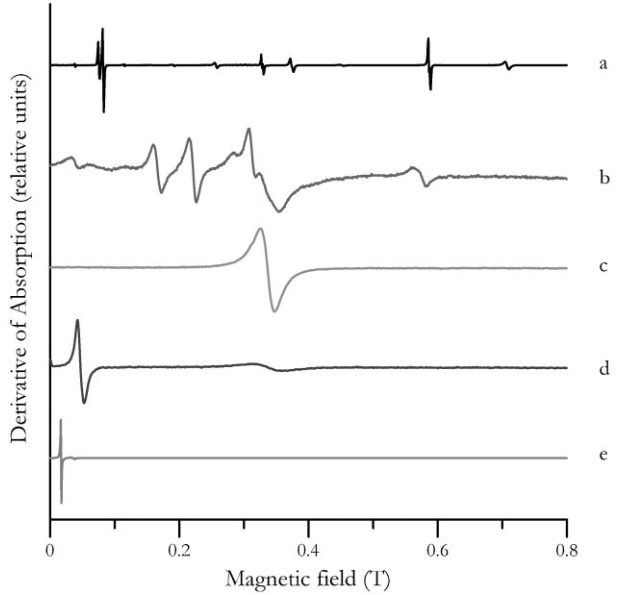


**Figure 2** Normalized derivative of absorption EMR spectra for  $\text{Fe}_x\text{Ga}_{1-x}\text{BO}_3$  crystals with different  $x$  values: 0.003 (a), 0.04 (b), 0.2 (c), 0.8 (d), and 1.0 (e).

been tentatively ascribed to iron nanoclusters. At still higher iron contents, curve d, besides the  $g_{\text{eff}} = 2.0$  line a new resonance emerges at low magnetic fields. Finally, at  $x = 1$  only the low-field resonance is observed, see curve e. The EMR in pure iron borate has been earlier identified as AFMR [20].

Below we present more detailed results for crystals with low Fe contents. Figure 3 (top) shows the EPR spectra of  $\text{Fe}_x\text{Ga}_{1-x}\text{BO}_3$  with  $x = 0.003$  at 4 K and different orientations of the magnetizing field  $B$ , described by a polar angle  $\vartheta$  with respect to the  $C_3$  axis and an azimuthal angle  $\varphi$  with respect to the  $C_2$  axis. Because of small crystal sizes, it was difficult to exactly determine their initial orientations in the resonant cavity. Therefore, the orientation angles have been considered as fitting parameters and refined through careful computer simulations. The accuracy of this procedure is confirmed by quality of the fittings obtained, cf. in Fig. 3 (bottom).

The spectra intensities at different temperatures closely follow the  $1/T$  Curie law. No temperature dependence of the resonance magnetic fields has been found.

In order to determine the EPR parameters, detailed computer simulations of the spectra recorded at different orientations of  $B$  have been carried out using a laboratory-developed code based on the conventional spin Hamiltonian of trigonal symmetry, containing Zeeman and fine-structure (fs) terms, e.g., see [26, 27]:

$$\mathcal{H} = g\beta\mathbf{B} \cdot \mathbf{S} + \frac{1}{3}DO_2^0 - \frac{1}{180}(a - F)O_4^0 + \frac{\sqrt{2}}{9}a(O_4^3 \cos 3\alpha \pm O_4^3 \sin 3\alpha), \quad (1)$$

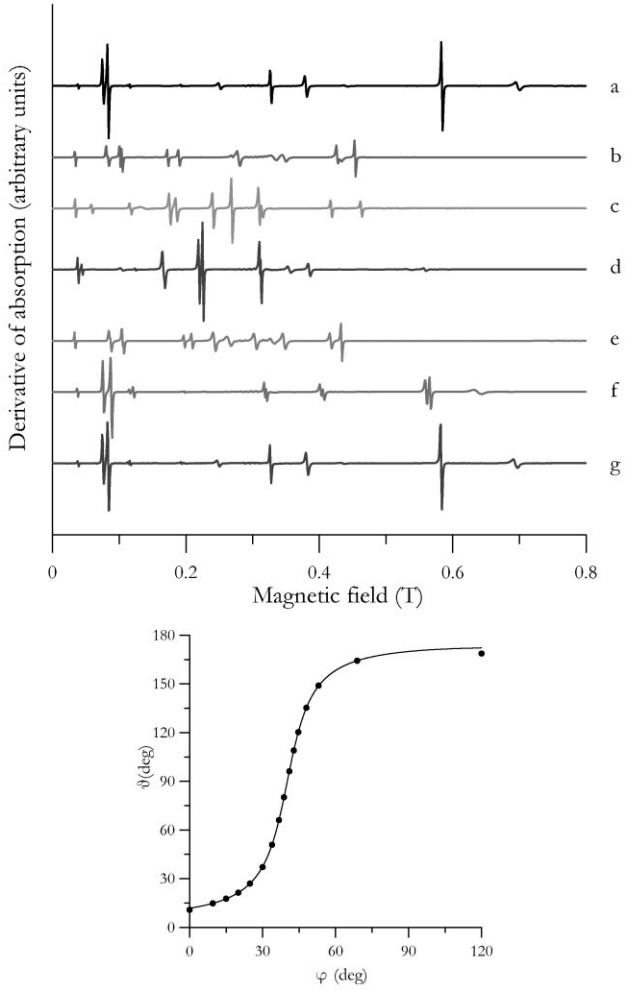


**Figure 3** Top: Experimental EPR spectra of  $\text{Fe}_x\text{Ga}_{1-x}\text{BO}_3$  crystal with  $x=0.003$  at 4 K for different orientations of  $B$ :  $\vartheta = 11^\circ$ ,  $\varphi = 0^\circ$  (a);  $\vartheta = 37^\circ$ ,  $\varphi = 30^\circ$  (b);  $\vartheta = 66^\circ$ ,  $\varphi = 37^\circ$  (c);  $\vartheta = 96^\circ$ ,  $\varphi = 41^\circ$  (d);  $\vartheta = 135^\circ$ ,  $\varphi = 48^\circ$  (e);  $\vartheta = 164^\circ$ ,  $\varphi = 69^\circ$  (f), and  $\vartheta = 169^\circ$ ,  $\varphi = 120^\circ$  (g). Bottom: relation between the spherical angles in the course of rotation of the crystal. Circles: spectra simulation results; full line: best fit curve calculated as  $\tan \vartheta = 0.12 / (0.57 \cos \varphi - 0.68 \sin \varphi)$ .

where  $g$  is close to the free electron  $g$ -factor,  $g_e = 2.0023$ ,  $\beta$  is the Bohr magneton,  $\mathbf{B}$  is the magnetizing field,  $\mathbf{S}$  is the electron spin for  $\text{Fe}^{3+}$  ion ( $S=5/2$ ),  $D$  is second-order axial fs parameter,  $a$  and  $F$  are, respectively, fourth-order cubic and axial fs parameters, and  $O_2^0$ ,  $O_4^0$ ,  $O_4^3$ , and  $O_4^3$  are extended Stevens operators as defined in Ref. [28]. Note that in Refs. [26–28] instead of  $O_4^3$  the notations  $\tilde{O}_4^3$ ,  $O_4^{3*}$ , and  $\Omega_4^3$  are used, respectively. The  $\pm$  signs in Eq. (1) refer to two magnetically non-equivalent  $\text{Fe}^{3+}$  sites with local magnetic axes rotated through the angle  $\pm\alpha$  about the  $C_3$  axis, see [26, 27].

First, we have focused on determining the sign of  $D$ , the leading parameter in Eq. (1). This could be achieved by following the temperature dependences of relative intensities of different resonance lines identified with transitions

between distinct spin levels. Figure 4 shows computer-generated spectra corresponding to different temperatures with  $a$  and  $F$  parameters set to zero in order to simplify the analysis. The various resonance lines in Fig. 4 are identified by the numbers of the spin levels involved in the corresponding transitions. (This identification is straightforward with our simulation code separating contributions of transitions between each pair of spin levels.) The most pronounced temperature dependence of the relative intensity occurs for the line located at 0.5717 T. One can see that as the temperature decreases, the relative intensity of this line increases for  $D > 0$  and decreases for  $D < 0$ . Figure 5 (top) shows a zoom of computer-generated spectra with positive  $D$  at two different temperatures. The comparison with the corresponding experimental spectra, see Fig. 5 (bottom), allows concluding that the sign of  $D$  is positive. (The splitting in Fig. 5 (bottom), instead of the single line in Fig. 5 (top), is observed because of the presence of two non-equivalent iron sites.)

After specifying the sign of  $D$ , its absolute value as well as exact values of  $a$  and  $F$  can be determined by accurate computer simulations of the experimental EPR spectra at different orientations of  $B$ , e.g., see Fig. 6. As a result, two different best-fit parameter sets have been obtained, as quoted in Table 1. The Set I parameters are in a reasonably good agreement with those obtained by Lukin et al. [26] for  $\text{Fe}_x\text{Ga}_{1-x}\text{BO}_3$  with nominal  $x$  value  $x=0.005$ , studied by EPR at Q- and V-bands (ca. 36 and 75 GHz, respectively).

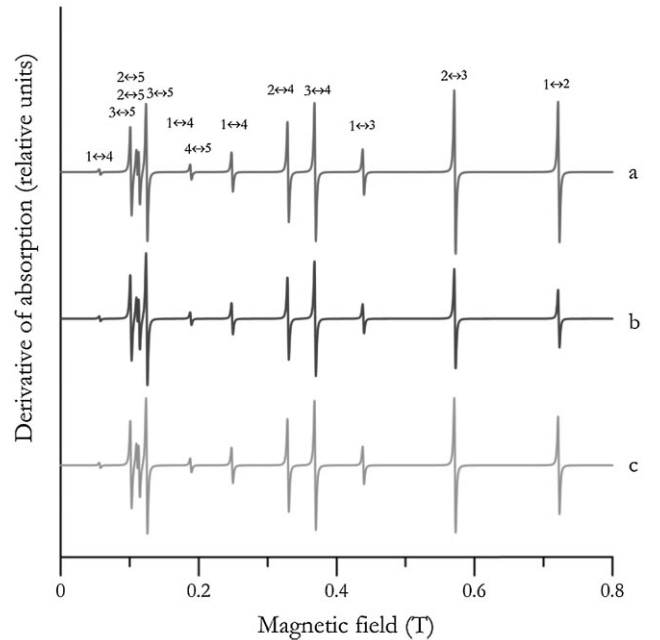


**Figure 4** Computer generated EPR spectra at 4 K with  $D > 0$  (a, red online) and  $D < 0$  (b, blue online) and at 300 K (c, green online). The parameters  $a$  and  $F$  are set to zero and the spectra intensities are multiplied by the absolute temperature. The numbering from 1 to 6 of the spin levels involved is in ascending order for  $D > 0$  and in descending order for  $D < 0$ .

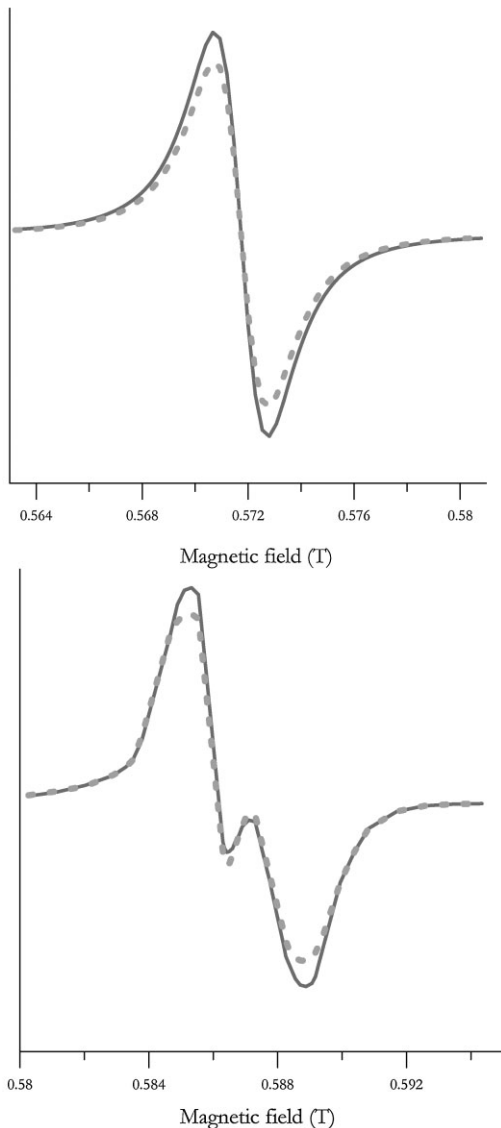


**Figure 5** Zooms of computer generated (top) and experimental (bottom) EPR spectra for  $\vartheta = 10^\circ$  and  $\varphi = 8^\circ$  at 4 (continuous, red online) and 30 K (dashed, green online). The spectra intensities have been multiplied by the absolute temperature.

As one can see from Fig. 6, the positions of different resonance lines are perfectly fitted to. Meanwhile, the relative amplitudes of certain lines are not satisfactorily reproduced in the simulations, in spite of the fact that both the positions and intensities of all resonance lines have been calculated from eigenvalues and eigenvectors determined within the same diagonalization procedure of the spin Hamiltonian matrix. This discrepancy will be discussed in the following section.

**4 Superposition model analysis of the spin Hamiltonian parameters** As far as both spin Hamiltonian parameter sets, see Table 1, result in one and the same

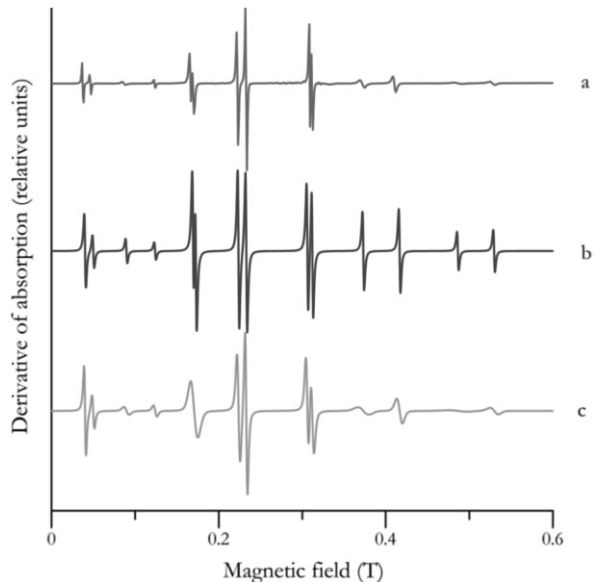


**Figure 6** Normalized experimental EPR spectrum of  $\text{Fe}_x\text{-Ga}_{1-x}\text{BO}_3$  with  $x=0.003$  at 4 K (a, red online), the best fit computer generated spectra for  $\vartheta = 80^\circ$  and  $\varphi = 39^\circ$  without (b, blue online) and with parameter distributions (c, green online). The simulation parameters for curve c are:  $b_2 = 0.4 \text{ cm}^{-1}$ ,  $t_2 = 8$ ,  $b_4 = 3.1 \times 10^{-5} \text{ cm}^{-1}$ ,  $t_4 = 5$ ,  $b_5 = 4.0 \times 10^{-6} \text{ cm}^{-1}$ ,  $t_5 = 7$ , see Eq. (6) and  $\sigma = 0.0005 \text{ \AA}$ .

spin Hamiltonian matrix, they can be considered as equivalent at least, from the mathematical viewpoint. Meanwhile, they may not necessarily be so from the physical viewpoint.

In order to elucidate this issue, we have tested the compatibility of both sets of parameters with the predictions of the Newman superposition model [29]. This semi-empirical model is based on a number of simplifying assumptions, see Ref. [30], in particular, that contributions from different metal-to-ligand bonds are axially symmetric and can be treated independently and that the characteristics of an individual bond are transferable across different crystals. These assumptions have been shown not to hold in the case of covalent bonding where changing metal-to-ligand distances or introducing a vacancy can modify the electronic density of the whole complex [31, 32]. Meanwhile, in iron-doped  $\text{GaBO}_3$  crystal, all ligands are located at the same distance from  $\text{Fe}^{3+}$  ion; besides, no structure defects are present in the close vicinity of the paramagnetic ion. Therefore, we can expect the superposition model to provide a more-or-less adequate first-approximation description of the  $\text{FeO}_6$  complex.

For the purpose of applying the superposition model, we have put forward a simulation code based on the general spin Hamiltonian for  $\text{Fe}^{3+}$  (see e.g., Ref. [28], p. 89):

$$\mathcal{H} = g\beta\mathbf{B} \cdot \mathbf{S} + \sum_{i=2}^2 B_2^i O_2^i + \sum_{i=4}^4 B_4^i O_4^i, \quad (2)$$

**Table 1** Spin Hamiltonian parameters for  $\text{Fe}^{3+}$  ions in  $\text{GaBO}_3$ ,  $g \approx 2.0023$ .

parameter	this work		Lukin et al. [26]
	set I	set II	
$D$ ( $\text{cm}^{-1}$ )	$0.1032 \pm 0.0005$	$0.1032 \pm 0.0005$	$0.0989 \pm 0.0049$
$a$ ( $\text{cm}^{-1}$ )	$0.0158 \pm 0.002$	$0.0158 \pm 0.002$	$0.0146 \pm 0.002$
$F$ ( $\text{cm}^{-1}$ )	$0.0052 \pm 0.002$	$0.0368 \pm 0.002$	$0.0052 \pm 0.003$
$\alpha$ ( $^\circ$ )	24	36	24

where  $O_2^j$  and  $O_4^j$  are the extended Stevens operators of appropriate superscripts. The second-order and fourth-order parameters of the spin Hamiltonians (2) and (1) are related to each other, respectively, as:

$$B_2^0 = \frac{1}{3}D \quad ; \quad B_2^2 = E \quad (3)$$

and

$$B_4^0 = \frac{1}{180}(F - a); \quad B_4^3 = \frac{\sqrt{2}}{9}a \cos 3\alpha; \quad (4)$$

$$B_4^3 = \pm \frac{\sqrt{2}}{9}a \sin 3\alpha.$$

In the framework of the Newman model, the  $B_l^m$  parameters are evaluated on the basis of a structural model of the paramagnetic site, as follows [29, 33]:

$$B_l^m = \sum_{j=1}^n b_l(r_j) K_l^m(\vartheta_j, \varphi_j). \quad (5)$$

In Eq. (5),  $j$  enumerates the nearest neighbours of the paramagnetic ion (ligands) with spherical coordinates  $r_j$ ,  $\vartheta_j$ , and  $\varphi_j$ ,  $b_l(r_j)$  are radial functions and  $K_l^m(\vartheta_j, \varphi_j)$  are coordination factors proportional to spherical harmonics with the corresponding  $l$  and  $m$  indices. The radial functions are expressed as power functions of the metal-to-ligand distances:

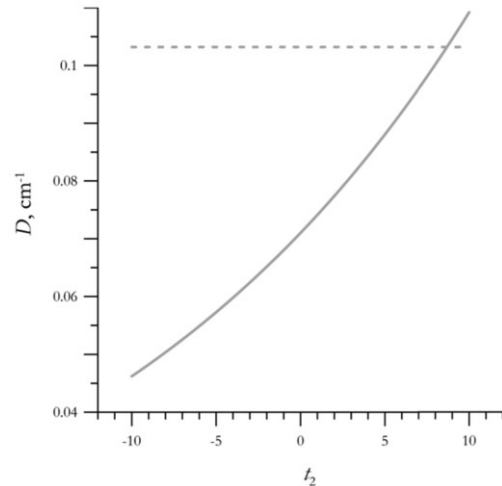
$$b_l(r_j) = b_l \times \left(\frac{r_0}{r_j}\right)^{t_l} \quad (6)$$

where the intrinsic parameters  $b_l$  and power exponents  $t_l$  are considered as fitting parameters. In applying Eqs. (5) and (6), the iron ligand coordinates have been calculated with structural parameters for both  $\text{FeBO}_3$  and  $\text{GaBO}_3$ , respectively. Meanwhile, as far as results of determination of  $b_l$  and  $t_l$  in both cases have been very close to each other, we have chosen to give all these results for ligand coordinates averaged between the  $\text{FeBO}_3$  and  $\text{GaBO}_3$  structures.

For  $\text{Fe}^{3+}$  in sixfold coordination, several second-order intrinsic parameter values are quoted in the literature. For the reference distance  $r_0 = 2.101 \text{ \AA}$  (corresponding to the average Fe O distance in  $\text{MgO}$  [34]), most often  $b_2 = -0.412 \text{ cm}^{-1}$  is taken, e.g., see Refs. [34, 35]. Meanwhile, a positive  $b_2 = 0.412 \text{ cm}^{-1}$  value has been assumed by

Acıkgöz et al. [36, 37]. The latter value has been adopted in the present case, as far as taking  $b_2 < 0$  would result in a negative  $D$  value, in disagreement with the experimental results. Figure 7 shows that for this choice, the agreement between the experimental and theoretical  $D$  values is attained with the second-order power exponent  $t_2 = 8.7$ , in a good agreement with the value  $t_2 = 8$  usually quoted for  $\text{Fe}^{3+}$  in oxygen environment, e.g., see [34, 35]. The calculated  $E$  values are close to zero, in accordance with the experimental results.

As only few references to the fourth-order intrinsic parameter values could be found in the literature, see Refs. [35, 38, 39], a large range of values has been tested for both  $b_4$  and  $t_4$  parameters. No consistent results could be obtained with negative  $b_4$  values. Figure 8 shows the dependence of  $a$  and  $F$  on  $t_4$  calculated for  $b_4 = 3.1 \times 10^{-5} \text{ cm}^{-1}$ . (This value of  $b_4$  is in a reasonable agreement with the value  $b_4 = 2.45 \times 10^{-5} \text{ cm}^{-1}$  for  $\text{Fe}^{3+}$  in calcite reported in Ref. [35].) One can see that in the framework of the Newman model the Set I parameters cannot be fitted to in the whole range of  $t_4$  values tested (Fig. 8, top). In contrast, for the Set II parameters, consistent results can be obtained with  $t_4 \approx 5$  for  $a$  and  $t_4 \approx 8$  for  $F$  (Fig. 8, bottom).

**Figure 7**  $D$  values versus the power exponent  $t_2$ . The dashed line is the  $D$  value determined from the experimental data, see Table 1.

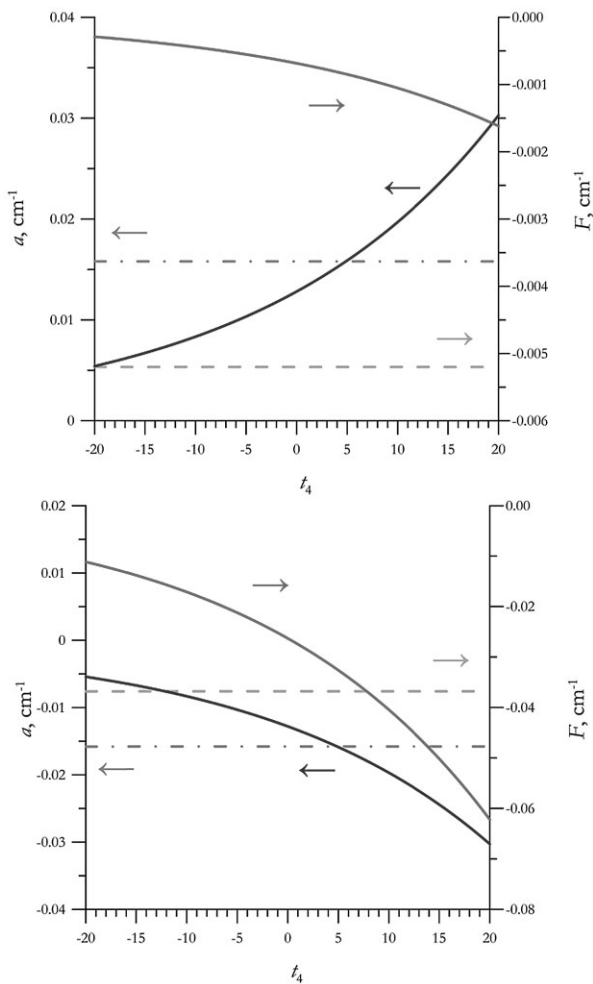


**Figure 8** Dependences of  $a$  (continuous, blue online) and  $F$  (continuous, red online) on the power exponent  $t_4$  for Set I (top) and Set II parameters (bottom). The experimental  $a$  and  $F$  values, see Table 1, are shown by the dash dotted (light blue online) and dashed lines (orange online), respectively.

Figure 9 shows the dependences of  $a$  and  $F$  on the intrinsic parameter  $b_4$  for different  $t_4$ . Once again, the Set II  $a$  and  $F$  parameters can be satisfactorily accounted for with close Newman model parameters; on the other hand, no agreement can be found for the Set I parameters. One can conclude that the Set I fourth-order fs parameters are totally incompatible with the predictions of the superposition model. In contrast, the Set II parameters can be quite consistently accounted for by this model. Thus, the spin Hamiltonian (1) is seen to be ambiguous; therefore, its use should be avoided. On the other hand, the spin Hamiltonian (2) has no such drawback.

Finally, we return to the discrepancy in relative line intensities in experimental and computer-generated spectra, see Fig. 6. This effect is a manifestation of a certain local disorder present in the crystals and resulting in statistical site-to-site distributions of the spin Hamiltonian parameters. As a consequence, a more or less pronounced broadening

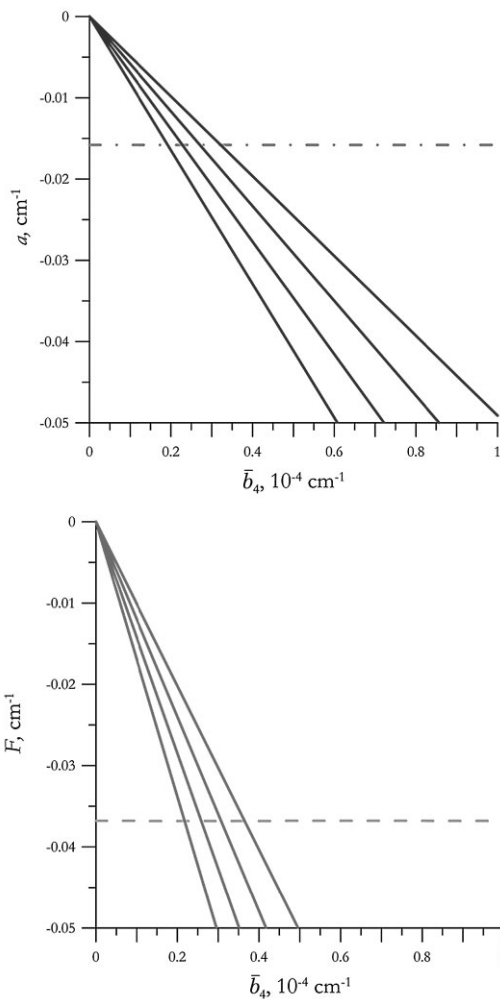


**Figure 9** Dependences of  $a$  (top) and  $F$  (bottom) on the intrinsic parameter  $b_4$  for different  $t_4$  values (4, 8, 12, and 16 from right to left, respectively) calculated with Set II spin Hamiltonian parameters. The horizontal lines show the Set II values of  $a$  (dash dotted, light blue online) and  $F$  (dashed, orange online).

and concomitant amplitude decrease are observed for the lines with stronger or weaker dependences of their resonance fields on these parameters.

In order to provide a more quantitative estimate of this effect, we have assumed that all the ligand coordinates undergo random site-to-site distributions. As a result, the spin Hamiltonian parameters will also be distributed. However, the latter distribution cannot be analysed in the framework of Eq. (1) because of the fact that in this case the local symmetry is lowered from the trigonal one. Moreover, strictly speaking, neither can it be analysed in the framework of Eq. (2) because the spin Hamiltonian expressed by means of the extended Stevens operators do not possess sufficient symmetry [40]. In order to overcome this difficulty, we have used a generalized spin Hamiltonian expressed by means of tesseral spherical tensor operators  $T_{lm}^{l_B l_S}(\mathbf{n}, \mathbf{S})$  where  $\mathbf{n}$  is the unit vector of the direction of  $\mathbf{B}$  and  $l_B$  and  $l_S$  are powers of  $\mathbf{B}$  and of the spin operators, respectively, e.g., see Ref. [40].

The spin Hamiltonian form needed can be adapted from Eq. (4) in Ref. [41], as follows, cf. [33]:

$$\mathcal{H} = \sum_{l=2,4} \sum_{m=-l}^l \mathcal{B}_{lm}^{0l} \mathcal{T}_{lm}(\mathbf{S}) + g_e \beta B \sum_{l_s=1,3,5} \sum_{l=\begin{cases} l_s-1 \\ l_{s+1} \end{cases}}^l \sum_{m=-l}^l \mathcal{B}_{lm}^{1l_s} \mathcal{T}_{lm}^{1l_s}(\mathbf{n}, \mathbf{S}). \quad (7)$$

Here the first and second terms in the right-hand side are, respectively, zero-field ( $l_B = 0$ ) and *linear Zeeman* ( $l_B = 1$ ) spin Hamiltonians;  $l$  must be even to preserve time-inversion invariance. The  $\mathcal{B}_{lm}^{0l}$  parameters in (7) are proportional to the corresponding Stevens parameters  $B_l^m$  [40], and the procedure of calculating the  $\mathcal{B}_{lm}^{1l_s}$  parameters is described in detail in the same work.

As far as  $\mathcal{B}_{lm}^{1l_s}$  are components of rank  $l$  irreducible tensors [40, 41], they can be consistently expressed within the superposition model, as follows [33]:

$$\mathcal{B}_{lm}^{1l_s} = \sum_{j=1}^n b_{lm}^{1l_s}(r_j) C_l^m(\vartheta_j, \varphi_j). \quad (8)$$

For simplicity, we assume that the radial functions in the latter equation depend only on  $l_B$  and  $l_S$  and have the radial dependence described in Eq. (6). The tesseral coordination factors  $C_l^m(\vartheta_j, \varphi_j)$  are given in Table A1, see Appendix.

The approach described above has the advantage of automatically taking into account the symmetry lowering brought by fluctuations of the ligand coordinates.

We have carried out some simulations of the EPR spectra using a laboratory-developed computer code, taking into account distributions of the ligand coordinates supposed to be Gaussian with standard deviation  $\sigma = 0.0005 \text{ \AA}$  and calculating the parameters of the spin Hamiltonian (7) by means of the superposition model. An example of such simulation is shown in Fig. 6 (curve c). One can see that in this model the relative intensities of various resonance lines are much better accounted for. More sophisticated models of the local disorder are expected to further improve the quality of fitting to the experimental EPR spectra. In any case, detailed computer fitting to the experimental EPR spectra reveals the presence of a certain degree of disorder in the environment of  $\text{Fe}^{3+}$  in gallium borate crystals.

**5 Conclusions and prospective** Mixed iron-gallium borates are exciting materials with unusual properties; indeed, depending on the composition, they can exhibit three magnetic phases, viz., paramagnetic, nanoclustered and long-range ordered (antiferromagnetic). In this work, we have focused only on the EPR of diluted  $\text{Fe}^{3+}$  ions in  $\text{GaBO}_3$ . Detailed computer simulations carried out with the conventional spin Hamiltonian have resulted in two different sets of the fourth-order spin Hamiltonian parameters, both yielding the same spin Hamiltonian matrix. This dichotomy has been resolved through testing the consistency

of both sets against the predictions of the Newman superposition model; indeed, only one set has proven to be compatible with the latter. Therefore, the use of the general spin Hamiltonian instead of the conventional one is highly recommended. Besides, the use of the general spin Hamiltonian in detailed simulations of the EPR spectra has allowed to conclude that some local disorder occurs in  $\text{Fe}_x\text{Ga}_{1-x}\text{BO}_3$  single crystals.

At higher  $x$  values, the characteristics of the EMR spectra of  $\text{Fe}_x\text{Ga}_{1-x}\text{BO}_3$  crystals become very complex, showing a gradual passage, first, from the EPR of diluted ions to the EMR of iron clusters and next, to the AFMR. The EMR studies of the corresponding phase transitions are in progress and will be published elsewhere.

**Acknowledgements** The authors are grateful to W.C. Tennant and D.G. McGavin for communicating some unpublished results on the relationship between the Stevens and tesseral spin Hamiltonian parameters and for valuable discussions.

## References

- [1] L. Bernal, C. W. Struck, and T. G. White, *Acta Crystallogr.* **16**, 849 (1963).
- [2] R. Diehl, *Solid State Commun.* **17**, 743 (1975).
- [3] R. Diehl, W. Jantz, B. I. Nolang, and W. Wettling, *Curr. Top. Mater. Sci.* **11**, 241 (1984).
- [4] M. Pernet, D. Elmach, and T. G. Toubert, *Solid State Commun.* **8**, 1583 (1970).
- [5] M. Eibschutz and M. E. Lines, *Phys. Rev. B* **7**, 4907 (1973).
- [6] A. M. Kalashnikova, A. V. Kimel, R. V. Pisarev, V. N. Gridnev, P. A. Usachev, A. Kirilyuk, and Th. Rasing, *Phys. Rev. B* **78**, 104301 (2008).
- [7] V. P. Glazkov, S. E. Kichanov, D. P. Kozlenko, B. N. Savenko, and V. A. Somenkov, *J. Magn. Magn. Mater.* **258**, 543 (2003).
- [8] K. Parlinski, J. Łażewski, P. T. Jochym, A. Chumakov, R. Rüffer, and G. Kresse, *Europhys. Lett.* **56**, 275 (2001).
- [9] E. M. Maksimova, I. A. Nauhatsky, M. B. Strugatsky, and V. E. Zubov, *J. Magn. Magn. Mater.* **322**, 477 (2010).
- [10] I. A. Troyan, M. I. Eremets, A. G. Gavriluk, I. S. Lyubutin, and V. A. Sarkisyan, *Pis'ma Zh. Eksp. Teor. Fiz.* **78**, 13 (2003).
- [11] A. M. Kalashnikova, A. V. Kimel, R. V. Pisarev, V. N. Gridnev, P. A. Usachev, A. Kirilyuk, and Th. Rasing, *Phys. Rev. Lett.* **99**, 167205 (2007).
- [12] I. S. Edelman, A. V. Malakhovskii, T. I. Vasileva, and V. N. Seleznyov, *Sov. Phys. Solid State* **14**, 2442 (1973).
- [13] A. V. Malakhovskii and I. S. Edelman, *Phys. Status Solidi B* **74**, K145 (1976).
- [14] W. Jantz, J. R. Sandercock, and W. Wettling, *J. Phys. C* **9**, 2229 (1976).
- [15] E. A. Turov, *Solid State Commun.* **87**, 1137 (1993).
- [16] M. B. Strugatsky, K. M. Skibinsky, V. V. Tarakanov, and V. I. Khizhnyi, *J. Magn. Magn. Mater.* **241**, 330 (2002).
- [17] M. B. Strugatsky and K. M. Skibinsky, *J. Magn. Magn. Mater.* **309**, 64 (2007).
- [18] M. Eibschutz, L. Pfeiffer, and J. W. Nielsen, *J. Appl. Phys.* **41**, 1276 (1970).
- [19] V. V. Tarakanov, V. I. Khizhnyi, A. P. Korolyuk, and M. B. Strugatsky, *Physica B* **284**, 1452 (2000).
- [20] L. V. Velikov, A. S. Prokhorov, E. G. Rudawevskii, and V. N. Seleznev, *Zh. Eksp. Teor. Fiz.* **66**, 1847 (1974).

- [21] M. B. Strugatsky, S. V. Yagupov, N. S. Postivey, K. A. Seleznyova, E. T. Milyukova, and V. S. Yagupov, *Sci. Notes of TNU (Simferopol) Ser. Phys. Math.* **24**(63), 169 (2011).
- [22] K. Seleznyova and A. Sukhachev, in: Abstracts of Int. Students, Postgraduates and Young Scientists Conf. "Lomonosov 2013", Moscow, Russia (2012).
- [23] I. Edelman, A. Malakhovskii, A. Sokolov, A. Sukhachev, V. Zabluda, S. Yagupov, M. Strugatsky, N. Postivey, and K. Seleznyova, in: Abstracts of Moscow Int. Symp. on Magnetism MISM 2011, Moscow, Russia (2011), p. 215.
- [24] I. Edelman, A. Malakhovskii, A. Sokolov, A. Sukhachev, V. Zabluda, S. Yagupov, M. Strugatsky, N. Postivey, and K. Seleznyova, *Funct. Mater.* (Kharkiv) **19**, 163 (2012).
- [25] S. V. Yagupov, M. B. Strugatsky, N. S. Postivey, K. A. Seleznyova, V. S. Yagupov, and E. T. Milyukova, in: Int. Conf. "Functional Materials" ICFM 2011, Partenit, Ukraine (2011), p. 184.
- [26] S. N. Lukin, V. V. Rudenko, V. N. Seleznev, and G. A. Tsintsadze, *Fiz. Tverd. Tela* **22**, 51 (1980).
- [27] V. Lupei, A. Lupei, and I. Ursu, *Rev. Roum. Phys.* **18**, 327 (1968).
- [28] S. A. Al'tshuler and B. M. Kozyrev, *EPR in Compounds of Transition Elements*, second ed. (John Wiley & Sons, New York/Toronto/Jerusalem/London, 1974), p. 512.
- [29] D. J. Newman and W. Urban, *J. Phys. C* **5**, 3101 (1972).
- [30] Y. Y. Yeung, *Superposition Model and its Applications*, in: *Optical Properties of 3d Ions in Crystals*, edited by N. M. Avram and M. G. Brik (Springer, Heidelberg, 2013).
- [31] M. Moreno, M. T. Barriuso, J. A. Aramburu, P. García Fernández, and J. M. García Lastra, *J. Phys.: Condens. Matter* **18**, R315 (2006).
- [32] J. A. Aramburu, P. García Fernández, M. T. Barriuso, and M. Moreno, *J. Phys. Chem. A* **117**, 12642 (2013).
- [33] J. Kliava and R. Berger, in: *Recent Research Developments in Non Crystalline Solids*, Vol. 3, edited by S. G. Pandalai (Transworld Research Network, Trivandrum, India, 2003), ISBN 81 7895 090 1, pp. 41-84.
- [34] E. Siegel and K. A. Muller, *Phys. Rev. B* **19**, 109 (1979).
- [35] D. J. Newman and E. Siegel, *J. Phys. C* **9**, 4285 (1976).
- [36] M. Acıkgöz, P. Gnutek, and C. Rudowicz, *Chem. Phys.* **402**, 83 (2012).
- [37] M. Acıkgöz, P. Gnutek, and C. Rudowicz, *Chem. Phys. Lett.* **524**, 49 (2012).
- [38] T. H. Yeom, *J. Phys.: Condens. Matter* **13**, 10471 (2001).
- [39] O. Rubio, S. Murrieta, and S. Aguilar, *J. Chem. Phys.* **71**, 4112 (1979).
- [40] D. G. McGavin, W. C. Tennant, and J. A. Weil, *J. Magn. Reson.* **87**, 92 (1990).
- [41] W. C. Tennant, C. J. Walsby, R. F. C. Claridge, and D. G. McGavin, *J. Phys.: Condens. Matter* **12**, 9481 (2000).

## Appendix

**Table A1** Tesseral coordination factors used in Eq. (8);  $x$ ,  $y$ , and  $z$  are the corresponding components of  $\mathbf{n}$ , the unit vector of the direction of  $\mathbf{B}$ , see Eq. (7).

$l$	$m$	$C_{lm}$	$l$	$m$	$C_{lm}$
2	0	$\frac{\sqrt{6}}{2}(3z^2 - 1)$	6	0	$\frac{\sqrt{231}}{4}(231z^6 - 315z^4 + 105z^2 - 5)$
	1	$3\sqrt{2}zx$		1	$6\sqrt{11}(33z^4 - 30z^2 + 5)zx$
	1	$3\sqrt{2}zy$		1	$6\sqrt{11}(33z^4 - 30z^2 + 5)zy$
	2	$\frac{3}{\sqrt{2}}(x^2 - y^2)$		2	$\frac{21\sqrt{110}}{8}(33z^4 - 18z^2 + 1)(x^2 - y^2)$
	2	$3\sqrt{2}xy$		2	$\frac{21\sqrt{110}}{4}(33z^4 - 18z^2 + 1)xy$
4	0	$\frac{\sqrt{70}}{4}(35z^4 - 30z^2 + 3)$	3	$\frac{21\sqrt{110}}{4}(x^2 - 3y^2)(11z^2 - 3)zx$	
	1	$5\sqrt{7}(7z^2 - 3)zx$	3	$\frac{21\sqrt{110}}{4}(3x^2 - y^2)(11z^2 - 3)zy$	
	1	$5\sqrt{7}(7z^2 - 3)zy$	4	$\frac{21\sqrt{33}}{4}(x^4 - 6x^2y^2 + y^4)(11z^2 - 1)$	
	2	$5\sqrt{\frac{7}{2}}(7z^2 - 1)(x^2 - y^2)$	4	$21\sqrt{33}(x^2 - y^2)(11z^2 - 1)xy$	
	2	$5\sqrt{14}(7z^2 - 1)xy$	5	$\frac{231\sqrt{6}}{4}(x^4 - 10x^2y^2 + 5y^4)zx$	
	3	$35(x^2 - 3y^2)zx$	5	$\frac{231\sqrt{6}}{4}(5x^4 - 10x^2y^2 + y^4)zy$	
	3	$35(3x^2 - y^2)zy$	6	$\frac{231\sqrt{2}}{8}(x^4 - 14x^2y^2 + 5y^4)(x^2 - y^2)$	
	4	$\frac{35\sqrt{2}}{4}(x^4 - 6x^2y^2 + y^4)$	6	$\frac{21\sqrt{110}}{4}(x^2 - 3y^2)(11z^2 - 3)zx$	
	4	$35\sqrt{2}(x^2 - y^2)xy$			